JOURNAL OF SOLID STATE CHEMISTRY **131,** 24–37 (1997)
ARTICLE NO. SC977295

An XRD and Electron Diffraction Study of Cristobalite-Related Phases in the $NaAlO_2$–$NaAlSiO_4$ System

John G. Thompson,[1] Alexandra Melnitchenko, Stephen R. Palethorpe, and Ray L. Withers

Research School of Chemistry, Australian National University, Canberra, ACT 0200, Australia

Received October 31, 1996; in revised form January 21, 1997; accepted January 27, 1997

A detailed study of the sodium aluminate–carnegieite system ($Na_{2-x}Al_{2-x}Si_xO_4$, $0 \le x \le 1$) at temperatures between 800 and 1300°C has revealed five previously unreported phases. All of the new phases can be described as modulated variants of an underlying β-cristobalite parent structure. At $x \approx 0.05$ the γ-$NaAlO_2$-type structure ($P4_12_12$, $a = 1/\sqrt{2}a_p$, $c = c_p$) (p = parent) is stabilized to room-temperature; at $x \approx 0.2$–0.45 an orthorhombic ($Pbca$, $a = \sqrt{2}a_p$, $b = 2b_p$, $c = 1/\sqrt{2}c_p$) $KGaO_2$-type structure is obtained, except at $x \approx 0.35$ where a new tetragonal ($P4_12_12$, $a = \sqrt{2}a_p$, $c = c_p$) phase is observed; at $x \approx 0.5$–0.6 a new cubic ($P2_13$, $a = 2a_p$) phase is obtained; at $x \approx 0.7$–0.9 a new orthorhombic ($Pc2_1b$, $a = \sqrt{2}a_p$, $b = 2b_p$, $c = \sqrt{2}c_p$) phase is obtained. XRD and electron diffraction data, refined unit cell dimensions, and the phase relationships at 1300°C are presented. The proposed space group symmetries are based on observed extinction conditions and constraints provided by a modulated structure description of the new phases. The materials are prepared by gel synthesis followed by solid state reaction in air.

INTRODUCTION

The ternary system Na_2O–Al_2O_3–SiO_2 has been intensively investigated over many decades because of its fundamental importance to a broad range of disciplines and technologies, including mineralogy, silicate ceramics, window glass, solid electrolytes, and synthetic zeolites. Despite the importance of the system it appears that there has been no systematic investigation of the pseudobinary $NaAlO_2$–$NaAlSiO_4$. The only reported phase diagram which includes this join as a function of temperature (1) implies a continuous solid solution extending between the end members $NaAlO_2$ and $NaAlSiO_4$.

The end members of this system, however, have enjoyed significant attention. $NaAlO_2$ is known to have four structural polymorphs. The low-temperature, low-pressure β form (Fig. 1c) is isostructural with β-$NaFeO_2$ and has orthorhombic symmetry (S.G. $Pna2_1$; $a = 5.3871(2)$, $b = 7.0320(2)$, $c = 5.2180(2)$ Å) (2). On heating above 470°C, β-$NaAlO_2$ undergoes a reversible nonreconstructive phase transition to its higher symmetry tetragonal γ form (S.G. $P4_12_12$; $a = 5.325$, $c = 7.058$ Å) (3), which is isostructural with γ-$NaFeO_2$. Above $\sim$1600°C to the melting point at $\sim$1650°C, the stable form is δ-$NaAlO_2$ (4) which is presumably the analogue of the high-temperature cubic polymorph δ-$NaFeO_2$ reported by Grey and Li (5), though details about δ-$NaAlO_2$ are sketchy. α-$NaAlO_2$ exists as the high-pressure polymorph and has a rhombohedrally distorted sodium chloride-type structure (S.G. $R\bar{3}m$; $a = 2.868(5)$, $c = 15.88(1)$, hexagonal setting) (6), isostructural with α-$NaFeO_2$, though the ferrite, unlike the aluminate, is the stable room-temperature polymorph at 1 atmosphere (7).

The β and γ forms of $NaAlO_2$, and presumably δ also, can be considered as structurally related to the high-temperature silica polymorph, β-cristobalite (S.G. $Fd\bar{3}m$; $a = 7.13$ Å) (8), shown in Figs. 1b and 2, also known as the C9 structure type (9). In fact, the AlO_2 framework of γ-$NaAlO_2$ is isostructural with the low-temperature form of cristobalite, namely the α form (S.G. $P4_12_12$; $a = 4.9732(4)$, $c = 6.9236(8)$ Å) (10), while the structure of β-$NaAlO_2$ can also be derived by appropriate distortion of its high-temperature polymorph.

At the other end of the subject binary system, $NaAlSiO_4$ has the nepheline structure as its thermodynamically stable form below 1250°C (1). Nepheline is structurally related to the silica polymorph tridymite. Above 1250°C to its melting point at 1526 ± 2°C (1) the stable polymorph of $NaAlSiO_4$ is carnegieite. High-carnegieite has a simple cubic structure with space group symmetry $P2_13$ or $F\bar{4}3m$ with unit cell dimension $a = 7.37(2)$ Å (11, 12). On cooling to room temperature relatively quickly (e.g., 1 minute) high-carnegieite undergoes a nonreconstructive phase transition at 667 ± 5°C (13) to its low-temperature orthorhombic form (S.G. $Pb2_1a$; $a = 10.261(1)$, $b = 14.030(2)$, $c = 5.1566(6)$ Å) (14, 15) (see Fig. 1a).

As with $NaAlO_2$, the high- and low-temperature forms of carnegieite are structurally related to β-cristobalite. Buerger

[1] To whom correspondence should be addressed.

0022-4596/97 $25.00

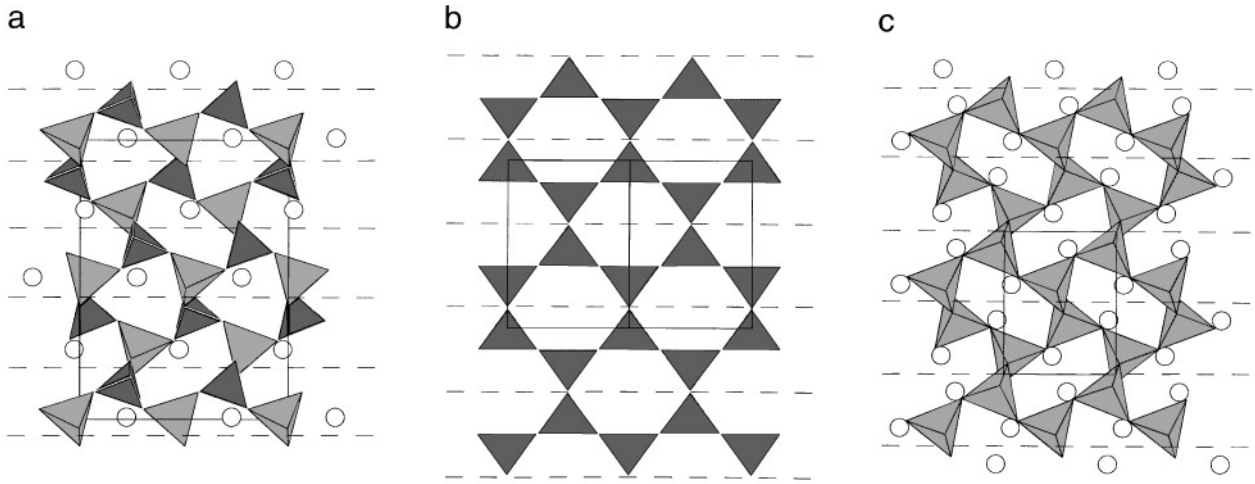

FIG. 1. Schematic polyhedral representations of (a) low-carnegieite and (c) γ-$NaAlO_2$ projected along their respective [001] directions juxtaposed to (b) the parent β-cristobalite structure projected along its [110] direction. Si and Al atoms are located at the center of the darker and lighter tetrahedra, respectively, with oxygen atoms at the vertices. The open circles represent the interstitial sodium atoms. The unit cells of the structures are indicated by the solid lines. The horizontal dashed lines emphasize the $\langle 110 \rangle$ strings of tetrahedra characteristic of all β-cristobalite-related structures.

(16) described carnegieite as a "stuffed" derivative of cristobalite in that the sodium atoms occupy the interstices in the tetrahedral framework. Withers and Thompson (14) showed that there is exact ordering of the Si and Al atoms in the tetrahedral framework of low-carnegieite, with the framework charge-balancing sodium atoms occupying half the interstices in an ordered manner. The same description as "stuffed" cristobalite is appropriate for the $NaAlO_2$ polymorphs except that the interstitial sites are now fully occupied and no framework atom ordering is possible. An alternative description of the $NaAlO_2$ structure is as an ordered wurtzite-type superstructure, in which Na and Al atoms are ordered over one set of tetrahedral sites within a hexagonal close-packed array of oxygens (5).

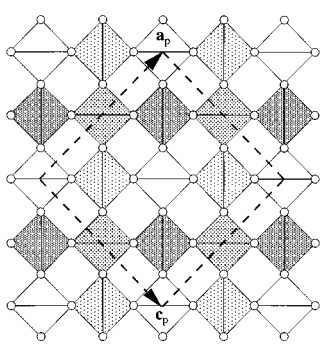

FIG. 2. Schematic polyhedral representation of the $Fd\bar{3}m$ C9 parent structure of ideal β-cristobalite projected along the [010] direction. Oxygen atoms at the vertices of the SiO_4 tetrahedra are represented by open circles. The parent unit cell is indicated by the dashed arrows. The shading of the tetrahedra represents different heights along $\mathbf{b}_p$.

While there appears to have been no systematic study of the pseudobinary $NaAlO_2$–$NaAlSiO_4$, the $NaFeO_2$–SiO_2 system has been investigated from 0–20 mol% SiO_2 (5). The study showed that the lower-temperature γ and β polymorphs of $NaFeO_2$ formed limited solid solutions with SiO_2, containing up to 5 and 11 mol% SiO_2, respectively, and that a new orthorhombic solid solution, designated γ'_{ss}, extended from 7.5 to beyond 20 mol SiO_2. A subsequent Rietveld refinement of this γ'_{ss} phase showed it to have space group symmetry *Pbca* and to be isostructural with $KGaO_2$ (17). Withers and Thompson (14) observed the close relationship between this γ'_{ss} phase and low-carnegieite in that the latter structure could be derived from the former simply by appropriate ordering of the tetrahedral and stuffing atoms. This relationship had been recognized previously by Grins and Louër (18) for $A_2M'M''O_4$ compounds with stuffed cristobalite structures.

One of the difficulties in achieving equilibrium in the synthesis of crystalline alkali aluminosilicates and their ferrite analogues in the solid state is the sluggish reaction kinetics. However, heating specimens at higher temperatures and/or for longer times to circumvent this results in loss of the alkali (5, 15). The difficulty in achieving equilibrium increases with increasing silica content, as described for the synthesis of fully ordered carnegieite (15). Consequently, it is preferable to use a sol–gel synthesis

approach to achieve the most intimate mixing of components prior to the pelleting–firing–grinding cycle described in the synthesis section of this study.

The present study employs a modulation wave approach to the description of the subject phases as all the structures are β-cristobalite-related; i.e., the resultant structures are described in terms of a β-cristobalite-type parent structure modulated by composition and/or displacive modulation waves associated with a limited number of independent modulation wave vectors. The main advantage of this approach over conventional superstructure descriptions is that the similarities and differences between the various structures are immediately apparent even though unit cell dimensions and space group symmetries appear unrelated. In each case the raw X-ray powder and electron diffraction data are dominated by the parent β-cristobalite reflections, with the structures being distinguished by their weaker satellite reflections. If one were to concentrate solely on the stronger parent reflections one might conclude that, indeed, a continuous solid-solution extends from $NaAlO_2$ to $NaAlSiO_4$!

The main objective of this present study has been to determine the phase equilibria on the pseudobinary join $NaAlO_2$–$NaAlSiO_4$ by careful synthesis and thorough characterization using X-ray powder and electron diffraction.

SYNTHESIS

As problems in reaching equilibrium were anticipated a preliminary study was undertaken to identify the best method of synthesis across the composition range. The three general methods were as follows:

(1) Adding colloidal silica to aqueous sodium aluminate and aluminium nitrate to form a gel, dehydrating the gel then grinding, pelleting, and firing.

(2) Adding colloidal silica to a concentrated aqueous solution of sodium and aluminium nitrates to form a gel, dehydrating the gel then grinding, pelleting, and firing.

(3) Thorough mixing of sodium silicate, sodium carbonate, and aluminium hydroxide as a slurry, dehydration of the slurry then grinding, pelleting, and firing.

Firing of specimens of the same composition under identical conditions showed that the second method gave the most complete reaction. Complete details of the synthesis using this method are now given.

Specimens were prepared at compositions $x = 0.05$, 0.15, 0.25, 0.35, 0.45, 0.5, 0.55, 0.65, 0.75, 0.85, 0.95, and 1.00 in the system $Na_{2-x}Al_{2-x}Si_xO_4$. Reagents used were LR grade $NaNO_3$ (Unilab, Ajax) and AR grade $Al(NO_3)_3 \cdot 9H_2O$ (AnalaR, BDH), and colloidal silica (Ludox AM, du Pont) containing 32.3 wt% SiO_2. In each case a gel of the required stoichiometry was prepared by adding colloidal silica to a concentrated, stirred solution of $Al(NO_3)_3 \cdot 9H_2O$ and $NaNO_3$, with continued stirring for 15–20 min. The gels were then dehydrated at 120°C overnight then heated in a Pt vessel at 700°C for 1.5 h. The resultant white solids were then ground into fine powders, pressed into pellets, and fired in air sequentially at 800, 1000, 1200, and 1300°C, typically for several days, with thorough grinding and repelleting between firings. It was observed during the preliminary study that specimens annealed at temperatures above ~1300°C led to significant Na loss as indicated by the formation of relatively Na-deficient β and β'' aluminas, phases which imply that the bulk composition has deviated from the binary join. Consequently, 1300°C was chosen as the upper limit of synthesis with a further cycle of grinding, pelleting, and firing to produce well-crystallized specimens where necessary.

For $x = 0.0$, i.e., $NaAlO_2$, the specimen was prepared by firing 99.9% grade sodium aluminate (Strem Chemicals) in air at 200°C overnight. Conditions of synthesis for all specimens with data presented in this study are summarized in Table 1, with the equilibrium specimens which are described in detail in this study in square brackets.

CHARACTERIZATION

Specimens were examined after each firing by X-ray powder diffraction (XRD) using a Siemens D5000 diffractometer with Cu$K\bar{\alpha}$ radiation ($\lambda = 1.5418$ Å). Having obtained equilibrium specimens the XRD data were

TABLE 1
Conditions of Synthesis

x[a]	Colloidal silica (g)[b]	Firing Time (days)[c] 1000°C	1200°C	1300°C	1300°C	1400°C
0.05	0.279	[2]	3	2	—	—
0.15	0.836	2	3	[2]	—	—
0.25	1.395	2	3	[2]	—	—
0.35	1.952	2	3	[2]	—	—
0.45	2.510	2	3	[2]	3	—
0.50	2.790	2	3	2	[3]	—
0.55	3.066	2	3	[2]	—	—
0.65	3.626	2	4	[3]	—	—
0.75	4.184	2	4	[3]	—	—
0.85	4.741	2	4	[3]	—	—
0.95	5.299	2	4	3	—	$\frac{2}{3}$
1.00	5.578	2	4	3	—	$\frac{2}{3}$

[a] x as in $Na_{2-x}Al_{2-x}Si_xO_4$.

[b] Amount of colloidal silica added to a solution of 2.55 g $NaNO_3$ and 11.25 g $Al(NO_3)_3 \cdot 9H_2O$ in 7 ml of H_2O at 35–40°C.

[c] Each specimen was ground and pelletized prior to each firing stage. Specimens for which data are presented in this study are in square brackets.

recollected using a Guinier–Hägg camera with monochromated Cu$K\alpha_1$ radiation ($\lambda = 1.5406$ Å) with Si (NBS No. 640) as an internal standard. The improved resolution due to the focussing geometry of the Guinier–Hägg camera enabled the extraction of very accurate peak positions which assisted in the indexing of data and the subsequent least-squares refinement of unit cell dimensions.

Selected area electron diffraction patterns (SAEDP's) from equilibrium specimens were then obtained using a JEOL 100CX transmission electron microscope (TEM). Finely ground specimen was dispersed onto a holey carbon grid for examination in the TEM.

RESULTS AND DISCUSSION

X-Ray Powder Diffraction

XRD data for specimens rapidly quenched to room temperature revealed five previously unreported phases in the sodium aluminate–carnegieite system ($Na_{2-x}Al_{1-x}Si_xO_4$, $0 \leq x \leq 1$). The XRD profiles for selected single-phase or predominantly single-phase specimens ($x = 0.05$, 0.25, 0.35, 0.45, 0.55, and 0.85) are shown in Figs. 3 and 4, together with the profiles for the β-cristobalite-related end members, β-$NaAlO_2$ ($x = 0.0$) and $NaAlSiO_4$–carnegieite ($x = 1.0$).

The main features to note are the similarity of all the profiles in terms of the dominant reflections at 21–22°2θ and 33.5–36°2θ and that the rest of the reflections, except for the strong reflection at 30.5°2θ in the $x = 0.0$ and 0.05 specimens, are substantially weaker. The dominant reflections at 21–22°2θ and 33.5–36°2θ are due to the $\{111\}_p^*$ and $\{220\}_p^*$ (p = parent) reflections of an underlying $Fd\bar{3}m$, β-cristobalite-type, parent structure. Note that here and in the following text, except for the indexing of XRD data in Tables 2–7, we use $(hkl)^*$ to refer to the reciprocal lattice vector $h\mathbf{a}^* + k\mathbf{b}^* + l\mathbf{c}^*$ and $\{hkl\}^*$ to refer to the symmetry-equivalent set of such reciprocal lattice vectors.

The XRD profiles of equilibrium specimens at $x = 0.15$, 0.50 and 0.65 showed two-phase mixtures with the equilibrium specimen at $x = 0.75$ being from the same solid solution as $x = 0.85$. Specimens at $x = 0.95$ and 1.0 did not reach equilibrium despite extended heating and remixing at 1300°C, nor after shorter heating times at 1400°C. In both cases the XRD profiles contained a mixture of phases including low-carnegieite, reminiscent of those previously reported as a "multiphase specimen" in Fig. 3 and Table II of Ref. 15.

The differences between the various structures in the system $Na_{2-x}Al_{2-x}Si_xO_4$ are evident in the detail of the weaker satellite reflections, emphasized in Fig. 4 by four-times expansion of the vertical axis and truncation of the $\{111\}_p^*$ and $\{220\}_p^*$ reflections. The satellite reflections are labeled according to the modulation wave-vector type as given in the caption. The significance of this labeling is discussed later.

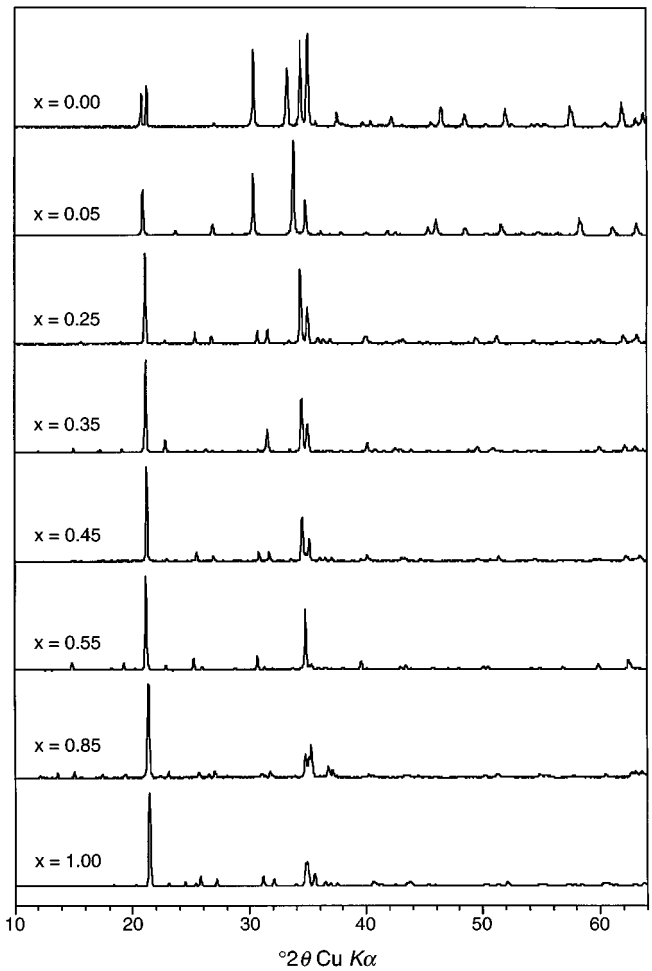

FIG. 3. X-ray powder diffraction profiles 10–64°2θ ($\lambda = 1.5418$ Å) for (a) $x = 0.0$, (b) $x = 0.05$, (c) $x = 0.25$, (d) $x = 0.35$, (e) $x = 0.45$, (f) $x = 0.55$, (g) $x = 0.85$ and (h) $x = 1.0$ in the system ($Na_{2-x}Al_{2-x}Si_xO_4$, $0 \leq x \leq 1$). Specimens $x = 0.25$, 0.35, 0.45, 0.55, and 0.85 had their final annealing at 1300°C, and $x = 0.0$ (β-$NaAlO_2$) and 0.05 at 1000°C. The profile for $x = 1.0$ (low-carnegieite) is calculated from the structure reported in Ref. (14).

Determination of Unit Cell and Space Group

Careful measurement of Guinier–Hägg films of the equilibrium specimens and comparison of adjacent specimens led to the identification of the correct unit cells for each new phase. The refined unit cell dimensions are listed in Table 8.

XRD data for the $x = 0.05$ specimen could be indexed to a primitive tetragonal ($a = 1/\sqrt{2}a_p$, $c = c_p$ (p = parent)) unit cell. The indexed reflections and their relative intensities, which are very similar to those reported data for γ-$NaAlO_2$ (3), are listed in Table 2.

The data for both the $x = 0.25$ and 0.45 specimens could be indexed to primitive orthorhombic ($a = \sqrt{2}a_p$, $b = 2b_p$, $c = 1/\sqrt{2}c_p$) unit cells. Indexing was assisted by comparison of the raw data with those reported for the γ'_{ss} phase in the

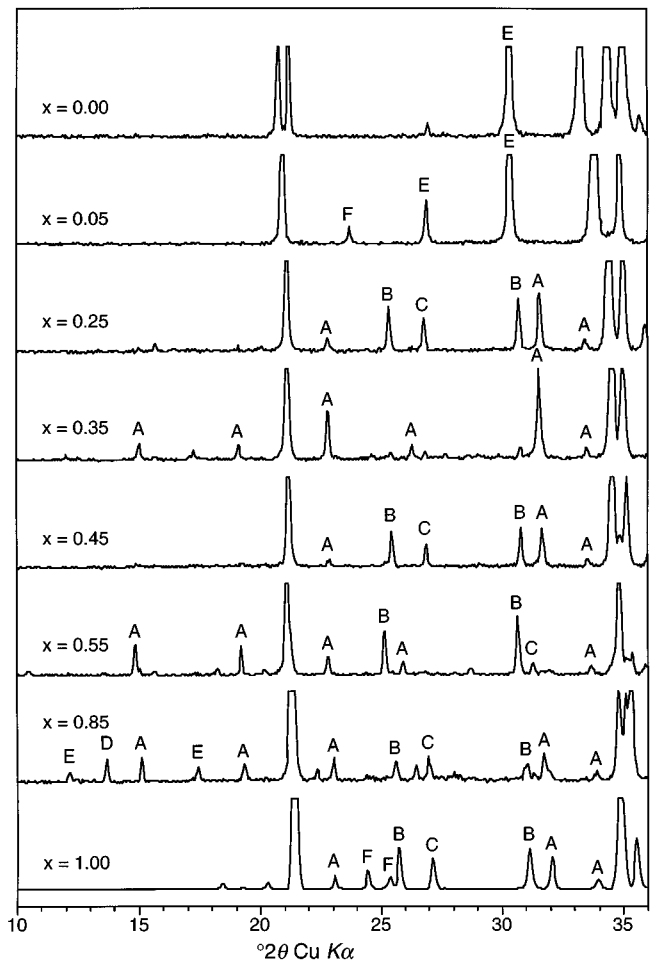

FIG. 4. X-ray powder diffraction profiles 10–36°2θ (as described in the legend for Fig. 3) with four-times expansion of the vertical axis and truncation of the $\{111\}_p^*$ and $\{220\}_p^*$ (p = parent) reflections. The satellite reflections are labeled according to the corresponding modulation wave-vector type with A = $\frac{1}{4}\{220\}^*$, B = $\frac{1}{4}\{002\}^*$, C = $\frac{1}{4}\{222\}^*$, D = $\frac{1}{4}\{024\}^*$, E = $\frac{1}{2}\{002\}^*$, and F = **0**.

$NaFeO_2$–SiO_2 system (5) and $Na_{1.74}Mg_{0.79}Al_{0.15}Si_{1.06}O_4$ (19), both of which are known to have the $KGaO_2$-type structure. The indexed reflections and their relative intensities are listed in Tables 3 and 5, respectively. Surprisingly, the data for the $x = 0.35$ specimen were qualitatively different from the $x = 0.25$ and 0.45 specimens and could be indexed to an enlarged primitive tetragonal ($a = \sqrt{2}a_p$, $c = c_p$) unit cell. The indexed reflections and their relative intensities are listed in Table 4.

At $x = 0.55$ the data were indexed to a large primitive cubic ($a = 2a_p$) unit cell, and at $x = 0.75$ and 0.85 the data could be indexed to a primitive orthorhombic ($a = \sqrt{2}a_p$, $b = 2b_p$, $c = \sqrt{2}c_p$) unit cell. Indexed reflections and relative intensities for the $x = 0.55$ and 0.85 specimens are listed in Tables 6 and 7, respectively.

TABLE 2

XRD Data for $x = 0.05$ in the System ($Na_{2-x}Al_{2-x}Si_xO_4$, $0 \le x \le 1$). Tetragonal, $P4_12_12$, $a = 1/\sqrt{2}a_p = 5.2997(6)$, $c = c_p = 7.0758(9)$ Å

No.	d_{obs} Å	d_{calc} Å	I/I_0	hkl	hkl_p	$\mathbf{G} + \mathbf{q}$
1.	4.24	4.24	50	101	111	111
2.	3.74	3.75	5	110	020	020
3.	3.31	3.31	13	111	021	$020 + \frac{1}{2}(002)$
4.	2.94	2.94	72	102	112	$111 + \frac{1}{2}(002)$
5.	2.65	2.65	100	200	220	220
6.	2.57	2.57	30	112	022	022
7.	2.483	2.482	4	201	221	$220 + \frac{1}{2}(002)$
8.	2.367	2.370	3	210	130	$131 - \frac{1}{2}(002)$
9.	2.249	2.247	3	211	131	131
10.	2.155	2.155	5	103	113	113
11.	2.119	2.121	3	202	222	222
12.	1.997	1.996	9	113	023	$022 + \frac{1}{2}(002)$
13.	1.970	1.969	17	212	132	$133 - \frac{1}{2}(002)$
14.	1.874	1.874	9	220	040	040
15.	1.811	1.811	2	221	041	$040 + \frac{1}{2}(002)$
16.	1.769	1.769	13	004	004	004
17.	1.762	1.762	2	203	223	$222 + \frac{1}{2}(002)$
18.	1.713	1.714	1	301	331	331
19.	1.677	1.676	1	310	240	240
20.	1.673	1.672	1	213	133	133
21.	1.657	1.656	1	222	042	042
22.	1.581	1.581	20	302	332	$331 + \frac{1}{2}(002)$
23.	1.515	1.515	9	312	242	242
24.	1.471	1.471	15	204	224	224
25.	1.418	1.418	—	214	134	$133 + \frac{1}{2}(002)$
26.	1.367	1.366	—	313	243	$242 + \frac{1}{2}(002)$
27.	1.286	1.285	—	410	350	$351 - \frac{1}{2}(002)$
28.	1.264	1.265	—	411	351	351
29.	1.216	1.217	—	314	244	244
30.	1.126	1.125	—	215	135	135
31.	1.125	1.125	—	116	026	026

Analysis of Phases in Terms of Modulation Waves

One of the advantages of using a modulation wave approach to the description of phases in the system ($Na_{2-x}Al_{2-x}Si_xO_4$, $0 \le x \le 1$) is that inspection of the XRD data allows identification of the dominant modulation wave or waves for each phase and easier comparison of phases. By reindexing all the satellite reflections in the XRD data relative to the parent structure as $\mathbf{G}_p \pm \mathbf{q}$, where $\mathbf{G}_p$ is an allowed β-cristobalite-type parent structure reflection and $\mathbf{q}$ is a modulation wave-vector (compare schematic representations in Figs. 5a and 5b with corresponding observed selected area electron diffraction patterns in Figs. 6a and 6b), it is now possible to make sense of the pattern of relative intensities of reflections for each phase. Note that compositional ordering associated with a $\mathbf{q} = \mathbf{0}$ modulation does not give rise to distinct satellite reflections on either side of parent reflections $\mathbf{G}_p$ but does put finite intensity into reflections forbidden by the d glide of the $Fd\bar{3}m$ parent (e.g.,

TABLE 3

XRD Data for $x = 0.25$ in the System ($Na_{2-x}Al_{2-x}Si_xO_4$, $0 \le x \le 1$). Orthorhombic, *Pbca*, $a = \sqrt{2}a_p = 10.4221(11)$, $b = 2b_p = 14.264(3)$, $c = 1/\sqrt{2}c_p = 5.2110(5)$ Å

No.	d_{obs} Å	d_{calc} Å	I/I_0	hkl	hkl_p	$\mathbf{G}+\mathbf{q}$
1.	4.21	4.21	100	220, 021	111, $\bar{1}11$	111, $\bar{1}11$
2.	3.91	3.90	4	121	$-\frac{1}{2}1\frac{3}{2}$	$\bar{1}11+\frac{1}{4}(202)$
3.	3.51	3.51	13	230	$1\frac{3}{2}1$	$111+\frac{1}{4}(020)$
4.	3.33	3.33	8	131	$-\frac{1}{2}\frac{3}{2}\frac{3}{2}$	$\bar{1}11+\frac{1}{4}(222)$
5.	2.91	2.91	15	231	$0\frac{3}{2}2$	$022+\frac{1}{4}(0\bar{2}0)$
6.	2.83	2.83	17	141	$-\frac{1}{2}2\frac{3}{2}$	$022+\frac{1}{4}(\bar{2}0\bar{2})$
7.	2.68	2.68	3	321	$\frac{1}{2}1\frac{5}{2}$	$113+\frac{1}{4}(\bar{2}0\bar{2})$
8.	2.61	2.61	83	002, 400	$\bar{2}02$, 202	$\bar{2}02$, 202
9.	2.56	2.56	40	241	022	022
10.	2.50	2.50	8	250	$1\frac{5}{2}1$	$131+\frac{1}{4}(0\bar{2}0)$
11.	2.470	2.470	7	331	$\frac{1}{2}\frac{3}{2}\frac{5}{2}$	$113+\frac{1}{4}(\bar{2}2\bar{2})$
12.	2.433	2.433	7	151	$-\frac{1}{2}\frac{5}{2}\frac{3}{2}$	$\bar{1}31+\frac{1}{4}(2\bar{2}2)$
13.	2.383	2.383	1	122	$-\frac{3}{2}1\frac{5}{2}$	$\bar{1}13+\frac{1}{4}(\bar{2}0\bar{2})$
14.	2.284	2.285	<1	430	$2\frac{3}{2}2$	$222+\frac{1}{4}(0\bar{2}0)$
15.	2.257	2.256	9	251	$0\frac{5}{2}2$	$022+\frac{1}{4}(020)$
16.	2.246	2.246	8	341	$\frac{1}{2}2\frac{5}{2}$	$022+\frac{1}{4}(202)$
17.	2.163	2.163	2	260, 061	131, $\bar{1}31$	131, $\bar{1}31$
18.	2.117	2.118	3	161	$-\frac{1}{2}3\frac{3}{2}$	$\bar{1}31+\frac{1}{4}(202)$
19.	2.104	2.104	4	440, 042	222, $\bar{2}22$	222, $\bar{2}22$
20.	2.093	2.093	5	232	$\bar{1}\frac{3}{2}3$	$\bar{1}13+\frac{1}{4}(020)$
21.	2.065	2.063	1	312	$-\frac{1}{2}\frac{1}{2}\frac{7}{2}$	$\bar{1}13+\frac{1}{4}(2\bar{2}2)$
22.	2.030	2.031	2	351	$\frac{1}{2}\frac{5}{2}\frac{5}{2}$	$133+\frac{1}{4}(\bar{2}\bar{2}\bar{2})$
23.	2.002	2.001	2	322	$-\frac{1}{2}1\frac{7}{2}$	$\bar{1}13+\frac{1}{4}(202)$
24.	1.843	1.842	7	402	004	004
25.	1.805	1.805	2	252,	$\bar{1}\frac{5}{2}3$,	$\bar{1}33+\frac{1}{4}(0\bar{2}0)$,
				451	$1\frac{5}{2}3$	$133+\frac{1}{4}(0\bar{2}0)$
26.	1.782	1.783	8	271, 080	$0\frac{7}{2}2$, 040	$042+\frac{1}{4}(0\bar{2}0)$, 040
27.	1.732	1.732	1	261	032	$022+\frac{1}{2}(020)$
28.	1.716	1.718	1	432	$0\frac{3}{2}4$	$024+\frac{1}{4}(0\bar{2}0)$
29.	1.699	1.701	1	541	$\frac{3}{2}2\frac{7}{2}$	$224+\frac{1}{4}(\bar{2}0\bar{2})$
30.	1.687	1.687	5	280	141	$131+\frac{1}{2}(020)$
31.	1.664	1.664	1	262, 461	$\bar{1}33$, 133	$\bar{1}33$, 133
32.	1.612	1.612	2	133	$-\frac{5}{2}\frac{3}{2}\frac{7}{2}$	$\bar{3}13+\frac{1}{4}(222)$
33.	1.605	1.605	2	281	042	042
34.	1.585	1.585	1	090	$0\frac{9}{2}0$	$040+\frac{1}{4}(020)$
35.	1.558	1.557	4	233,	$\bar{2}\frac{3}{2}4$,	$\bar{2}24+\frac{1}{4}(0\bar{2}0)$,
				631	$2\frac{3}{2}4$	$224+\frac{1}{4}(0\bar{2}0)$
36.	1.544	1.544	6	143	$-\frac{5}{2}2\frac{7}{2}$	$224+\frac{1}{4}(20\bar{2})$
37.	1.533	1.534	2	272,	$\bar{1}\frac{7}{2}3$,	$\bar{1}33+\frac{1}{4}(020)$,
				471	$1\frac{7}{2}3$	$133+\frac{1}{4}(020)$
38.	1.517	1.518	1	381	$\frac{1}{2}4\frac{5}{2}$	$042+\frac{1}{4}(002)$
39.	1.496	1.496	9	243, 641	$\bar{2}24$, 224	$\bar{2}24$, 224
40.	1.483	1.484	1	650	$3\frac{5}{2}3$	$333+\frac{1}{4}(0\bar{2}0)$
41.	1.477	1.477	2	333	$-\frac{3}{2}\frac{3}{2}\frac{9}{2}$	$\bar{1}51+\frac{1}{4}(\bar{2}2\bar{2})$
42.	1.471	1.472	8	480, 082	242, $\bar{2}42$	242, $\bar{2}42$
43.	1.456	1.456	2	291	$0\frac{9}{2}2$	$042+\frac{1}{4}(020)$
44.	1.426	1.426	3	0 10 0	050	$040+\frac{1}{2}(020)$
45.	1.402	1.403	2	660	333	333
46.	1.389	1.390	1	391	$1\frac{9}{2}\frac{5}{2}$	$153+\frac{1}{4}(\bar{2}\bar{2}\bar{2})$
47.	1.382	1.383	2	433,	$\bar{1}\frac{3}{2}5$,	$\bar{1}15+\frac{1}{4}(020)$,
				632	$1\frac{3}{2}5$	$115+\frac{1}{4}(020)$

TABLE 4

XRD Data for $x = 0.35$ in the System $Na_{2-x}Al_{2-x}Si_xO_4$, $0 \le x \le 1$). Tetragonal, $P4_12_12$, $a = \sqrt{2}a_p = 10.3872(7)$, $c = c_p = 7.1589(8)$ Å

No.	d_{obs} Å	d_{calc} Å	I/I_0	hkl	hkl_p	$\mathbf{G}+\mathbf{q}$
1.	7.34	7.34	1	110	010	$000+\frac{1}{2}(020)$
2.	5.89	5.89	4	101	$\frac{1}{2}\frac{1}{2}1$	$111+\frac{1}{4}(\bar{2}\bar{2}0)$
3.	5.13	5.13	3	111	011	$111+\frac{1}{2}(\bar{2}00)$
4.	4.64	4.65	4	210	$\frac{1}{2}\frac{3}{2}0$	$020+\frac{1}{4}(2\bar{2}0)$
5.	4.20	4.20	100	201	111	111
6.	3.89	3.90	12	211	$\frac{1}{2}\frac{3}{2}1$	$111+\frac{1}{4}(\bar{2}20)$
7.	3.38	3.38	3	102	$\frac{1}{2}\frac{1}{2}2$	$002+\frac{1}{4}(220)$
8.	3.22	3.22	1	112	012	$002+\frac{1}{2}(020)$
9.	2.98	2.99	1	311	121	$111+\frac{1}{2}(020)$
10.	2.84	2.84	22	212	$\frac{1}{2}\frac{3}{2}2$	$022+\frac{1}{4}(2\bar{2}0)$
11.	2.67	2.67	3	321	$\frac{1}{2}\frac{5}{2}1$	$131+\frac{1}{4}(\bar{2}\bar{2}0)$
12.	2.60	2.60	57	400	220	220
13.	2.56	2.56	27	222	022	022
14.	2.52	2.52	<1	410	$\frac{3}{2}\frac{5}{2}0$	$220+\frac{1}{4}(\bar{2}20)$
15.	2.450	2.448	<1	330	030	$020+\frac{1}{2}(020)$
16.	2.423	2.420	1	312	122	$222+\frac{1}{2}(\bar{2}00)$
17.	2.376	2.376	1	411	$\frac{3}{2}\frac{5}{2}1$	$131+\frac{1}{4}(2\bar{2}0)$
18.	2.326	2.326	1	103	$\frac{1}{2}\frac{1}{2}3$	$113+\frac{1}{4}(\bar{2}\bar{2}0)$
19.	2.244	2.246	10	322	$\frac{1}{2}\frac{5}{2}2$	$022+\frac{1}{4}(220)$
20.	2.209	2.209	3	421	131	131
21.	2.169	2.168	1	203	113	113
22.	2.123	2.123	3	213	$\frac{1}{2}\frac{3}{2}3$	$113+\frac{1}{4}(\bar{2}20)$
23.	2.102	2.102	2	402	222	222
24.	2.060	2.060	2	412	$\frac{3}{2}\frac{5}{2}2$	$222+\frac{1}{4}(\bar{2}20)$
25.	1.995	1.996	1	431	$\frac{1}{2}\frac{7}{2}1$	$131+\frac{1}{4}(\bar{2}20)$
26.	1.959	1.959	<1	511	231	$131+\frac{1}{2}(200)$
27.	1.862	1.863	<1	521	$\frac{3}{2}\frac{7}{2}1$	$131+\frac{1}{4}(220)$
28.	1.836	1.837	9	440	040	040
29.	1.797	1.797	<1	432	$\frac{1}{2}\frac{7}{2}2$	$042+\frac{1}{4}(2\bar{2}0)$
30.	1.790	1.790	8	004	004	004
31.	1.779	1.779	2	441	041	$040+\frac{1}{2}(002)$
32.	1.732	1.732	2	431	$\frac{1}{2}\frac{7}{2}1$	$131+\frac{1}{4}(\bar{2}20)$
33.	1.699	1.699	1	522	$\frac{3}{2}\frac{7}{2}2$	$242+\frac{1}{4}(\bar{2}\bar{2}0)$
34.	1.683	1.683	2	601	331	331
35.	1.661	1.661	<1	611	$\frac{5}{2}\frac{7}{2}1$	$331+\frac{1}{4}(\bar{2}20)$
36.	1.542	1.541	11	612	$\frac{5}{2}\frac{7}{2}2$	$242+\frac{1}{4}(2\bar{2}0)$
37.	1.493	1.493	11	622	242	242
38.	1.474	1.474	10	404	224	224
39.	1.459	1.459	1	414	$\frac{3}{2}\frac{5}{2}4$	$224+\frac{1}{4}(\bar{2}20)$
40.	1.421	1.421	—	632	$\frac{3}{2}\frac{9}{2}2$	$242+\frac{1}{4}(\bar{2}20)$

002_p, 020_p). The effects of such a $\mathbf{q} = \mathbf{0}$ modulation could be accommodated by lowering the parent space group symmetry from $Fd\bar{3}m$ to $F\bar{4}3m$, but because we wish to relate all β-cristobalite-related structures to a common parent and to be consistent with earlier studies (14, 19) we have chosen the higher symmetry parent.

Throughout this section and in the Tables of XRD data, reflections are indexed in terms of the parent structure. Therefore the subscript p is omitted for brevity.

TABLE 5
XRD Data for $x = 0.45$ in the System $Na_{2-x}Al_{2-x}Si_xO_4$, $0 \le x \le 1$). Orthorhombic, *Pbca*, $a = \sqrt{2}a_p = 10.385(1)$, $b = 2b_p = 14.198(3)$, $c = 1/\sqrt{2}c_p = 5.1925(6)$ Å

No.	d_{obs} Å	d_{calc} Å	I/I_0	hkl	hkl_p	$\mathbf{G} + \mathbf{q}$
1.	4.19	4.19	100	220, 021	111, $\bar{1}11$	111, $\bar{1}11$
2.	3.89	3.89	3	121	$-\frac{1}{2}1\frac{3}{2}$	$\bar{1}11 + \frac{1}{4}(202)$
3.	3.49	3.50	10	230	$1\frac{3}{2}1$	$111 + \frac{1}{4}(020)$
4.	3.31	3.31	7	131	$-\frac{1}{2}\frac{3}{2}\frac{3}{2}$	$\bar{1}11 + \frac{1}{4}(222)$
5.	2.90	2.90	12	231	$0\frac{3}{2}2$	$022 + \frac{1}{4}(0\bar{2}0)$
6.	2.82	2.82	12	141	$-\frac{1}{2}2\frac{3}{2}$	$022 + \frac{1}{4}(\bar{2}0\bar{2})$
7.	2.67	2.67	2	321	$\frac{1}{2}1\frac{5}{2}$	$113 + \frac{1}{4}(\bar{2}0\bar{2})$
8.	2.60	2.60	48	002, 400	$\bar{2}02$, 202	$\bar{2}02$, 202
9.	2.55	2.55	25	241	022	022
10.	2.491	2.491	5	250	$1\frac{5}{2}1$	$131 + \frac{1}{4}(0\bar{2}0)$
11.	2.459	2.460	5	331	$\frac{1}{2}\frac{3}{2}\frac{5}{2}$	$022 + \frac{1}{4}(2\bar{2}2)$
12.	2.423	2.423	5	151	$-\frac{1}{2}\frac{5}{2}\frac{3}{2}$	$022 + \frac{1}{4}(\bar{2}2\bar{2})$
13.	2.275	2.276	2	430	$\bar{2}\frac{3}{2}2$	$\bar{2}22 + \frac{1}{4}(0\bar{2}0)$
14.	2.248	2.246	7	251	$0\frac{5}{2}2$	$022 + \frac{1}{4}(020)$
15.	2.237	2.237	<1	341	$\frac{1}{2}2\frac{5}{2}$	$022 + \frac{1}{4}(202)$
16.	2.153	2.153	1	260, 061	131, $\bar{1}31$	131, $\bar{1}31$
17.	2.110	2.108	4	161	$-\frac{1}{2}3\frac{3}{2}$	$\bar{1}31 + \frac{1}{4}(202)$
18.	2.097	2.096	4	440, 042	222, $\bar{2}22$	222, $\bar{2}22$
19.	2.086	2.085	4	232	$\bar{1}\frac{3}{2}3$	$\bar{1}13 + \frac{1}{4}(020)$
20.	2.021	2.022	2	351	$1\frac{5}{2}\frac{5}{2}$	$133 + \frac{1}{4}(\bar{2}2\bar{2})$
21.	1.995	1.994	1	322	$-\frac{1}{2}1\frac{7}{2}$	$\bar{1}13 + \frac{1}{4}(202)$
22.	1.836	1.836	3	402	004	004
23.	1.798	1.798	2	252	$\bar{1}\frac{5}{2}3$	$\bar{1}33 + \frac{1}{4}(0\bar{2}0)$
24.	1.775	1.775	7	271, 080	$0\frac{7}{2}2$, 040	$042 + \frac{1}{4}(0\bar{2}0)$, 040
25.	1.693	1.695	<1	541	$\frac{3}{2}2\frac{7}{2}$	$224 + \frac{1}{4}(\bar{2}0\bar{2})$
26.	1.682	1.682	3	620, 023	313, $\bar{3}13$	313, $\bar{3}13$
27.	1.626	1.626	1	630	$3\frac{3}{2}3$	$313 + \frac{1}{4}(020)$
28.	1.607	1.606	1	133	$-\frac{5}{2}\frac{3}{2}\frac{7}{2}$	$\bar{2}24 + \frac{1}{4}(\bar{2}2\bar{2})$
29.	1.598	1.598	1	470, 281	$2\frac{7}{2}2$, 042	$242 + \frac{1}{4}(0\bar{2}0)$, 042
30.	1.581	1.580	1	522, 172	$\frac{1}{2}1\frac{9}{2}$, $-\frac{3}{2}\frac{7}{2}\frac{5}{2}$	$115 + \frac{1}{4}(\bar{2}0\bar{2})$, $\bar{1}33 + \frac{1}{4}(\bar{2}2\bar{2})$
31.	1.551	1.551	2	233	$\bar{2}\frac{3}{2}4$	$\bar{2}24 + \frac{1}{4}(0\bar{2}0)$
32.	1.540	1.539	3	313	$-\frac{3}{2}\frac{1}{2}\frac{9}{2}$	$115 + \frac{1}{4}(2\bar{2}\bar{2})$
33.	1.527	1.528	<1	272	$\bar{1}\frac{7}{2}3$	$\bar{1}33 + \frac{1}{4}(020)$
34.	1.512	1.513	<1	323	$-\frac{3}{2}1\frac{9}{2}$	$\bar{1}15 + \frac{1}{4}(\bar{2}0\bar{2})$
35.	1.491	1.491	7	243	$\bar{2}24$	$\bar{2}24$

The XRD data for the primitive tetragonal phase at $x = 0.05$ can be indexed exclusively as parent structure reflections and $\mathbf{G} \pm \frac{1}{2}\{002\}^*$ satellite reflections (see Table 2 and reflections labeled E in Fig. 4), indicating that the important modulation wave for this phase has modulation wave-vector $\mathbf{q} = \mathbf{c}^*$. The primitive orthorhombic phase occurring at $x = 0.25$ and 0.45 is more complex in that the strong satellite data have three dominant satellite types associated with modulation wave-vectors, $\frac{1}{4}\{220\}^*$, $\frac{1}{4}\{002\}^*$, and $\frac{1}{4}\{222\}^*$ (see Tables 3 and 5) which are labeled A, B, and C, respectively, in Fig. 4. The primitive tetragonal phase at $x = 0.35$ straddled by this orthorhombic phase, however, is dominated by $\mathbf{G} \pm \frac{1}{4}\{220\}^*$-type satellite reflections (see Table 4) with the only other observed satellite reflections being relatively weak $\mathbf{G} \pm \frac{1}{4}\{002\}^*$ type.

TABLE 6
XRD Data for $x = 0.55$ in the System $Na_{2-x}Al_{2-x}Si_xO_4$, $0 \le x \le 1$). Cubic, $P2_13$ $a = 2a_p = 14.553(1)$ Å

No.	d_{obs} Å	d_{calc} Å	I/I_0	hkl	hkl_p	$\mathbf{G} + \mathbf{q}$
1.	8.39	8.40	1	111	$\frac{1}{2}\frac{1}{2}\frac{1}{2}$	$000 + \frac{1}{4}(222)$
2.	5.94	5.94	10	211	$1\frac{1}{2}\frac{1}{2}$	$111 + \frac{1}{4}(0\bar{2}\bar{2})$
3.	4.85	4.85	1	221, 300	$11\frac{1}{2}$,etc.	$111 + \frac{1}{4}(00\bar{2})$, etc.
4.	4.60	4.60	9	310	$\frac{3}{2}\frac{1}{2}0$	$200 + \frac{1}{4}(\bar{2}20)$
5.	4.40	4.40	1	311	$\frac{3}{2}\frac{1}{2}\frac{1}{2}$	$111 + \frac{1}{4}(\bar{2}22)$
6.	4.20	4.20	100	222	111	111
7.	3.89	3.89	6	321	$\frac{3}{2}1\frac{1}{2}$	$111 + \frac{1}{4}(20\bar{2})$
8.	3.53	3.53	13	322, 410	$\frac{3}{2}11$, etc	$111 + \frac{1}{4}(200)$, etc.
9.	3.43	3.43	4	330, 411	$\frac{3}{2}\frac{3}{2}0$, etc.	$220 + \frac{1}{4}(\bar{2}\bar{2}0)$, etc.
10.	3.10	3.10	1	332	$\frac{3}{2}\frac{3}{2}1$	$111 + \frac{1}{4}(220)$
11.	2.91	2.91	17	430, 500	$2\frac{3}{2}0$, etc.	$220 + \frac{1}{4}(0\bar{2}0)$, etc.
12.	2.80	2.80	1	333, 511	$\frac{3}{2}\frac{3}{2}\frac{3}{2}$, etc.	$222 + \frac{1}{4}(\bar{2}\bar{2}\bar{2})$, etc.
13.	2.66	2.66	2	521	$\frac{5}{2}1\frac{1}{2}$	$311 + \frac{1}{4}(\bar{2}0\bar{2})$
14.	2.57	2.57	70	440	220	220
15.	2.53	2.53	7	441, 522	$22\frac{1}{2}$, etc.	$220 + \frac{1}{4}(002)$, etc.
16.	2.496	2.496	3	433, 530	$2\frac{3}{2}\frac{3}{2}$, etc.	$222 + \frac{1}{4}(0\bar{2}\bar{2})$, etc.
17.	2.460	2.460	3	531	$\frac{5}{2}\frac{3}{2}\frac{1}{2}$	$220 + \frac{1}{4}(2\bar{2}2)$
18.	2.422	2.425	1	442, 600	221, etc.	$220 + \frac{1}{2}(002)$, etc.
19.	2.361	2.361	1	532, 611	$\frac{5}{2}\frac{3}{2}1$, etc.	$311 + \frac{1}{4}(\bar{2}20)$, etc.
20.	2.273	2.273	10	433, 540, 621	$22\frac{3}{2}$, etc.	$222 + \frac{1}{4}(00\bar{2})$, etc.
21.	2.246	2.246	1	541	$\frac{5}{2}2\frac{1}{2}$	$220 + \frac{1}{4}(202)$
22.	2.145	2.146	1	631	$3\frac{3}{2}\frac{1}{2}$	$311 + \frac{1}{4}(02\bar{2})$
23.	2.100	2.101	4	444	222	222
24.	2.080	2.079	5	632, 700	$3\frac{3}{2}1$, etc.	$311 + \frac{1}{4}(020)$, etc.
25.	2.058	2.058	1	543, 550, 710	$\frac{5}{2}2\frac{3}{2}$, etc.	$222 + \frac{1}{4}(20\bar{2})$, etc.
26.	2.037	2.038	<1	551, 711	$\frac{5}{2}\frac{5}{2}\frac{1}{2}$, etc.	$331 + \frac{1}{4}(\bar{2}\bar{2}\bar{2})$, etc.
27.	1.999	1.999	1	641, 720	$32\frac{1}{2}$, etc.	$311 + \frac{1}{4}(04\bar{2})$, etc.
28.	1.980	1.980	1	552, 633, 721	$\frac{5}{2}\frac{5}{2}1$. etc.	$331 + \frac{1}{4}(\bar{2}\bar{2}0)$, etc.
29.	1.928	1.928	<1	544, 722	$\frac{5}{2}22$, etc.	$222 + \frac{1}{4}(200)$, etc.
30.	1.911	1.911	<1	730	$\frac{7}{2}\frac{3}{2}0$	$420 + \frac{1}{4}(\bar{2}\bar{2}0)$
31.	1.894	1.895	<1	553, 731	$\frac{5}{2}\frac{5}{2}\frac{3}{2}$, etc.	$331 + \frac{1}{4}(\bar{2}\bar{2}\bar{2})$, etc.
32.	1.849	1.848	<1	651, 732	$3\frac{3}{2}\frac{1}{2}$, etc.	$331 + \frac{1}{4}(0\bar{2}\bar{2})$, etc.
33.	1.819	1.819	4	800	400	400
34.	1.805	1.805	3	652, 810, 740	$3\frac{5}{2}1$, etc.	$331 + \frac{1}{4}(0\bar{2}0)$, etc.
35.	1.790	1.791	<1	554, 741, 811	$\frac{5}{2}\frac{5}{2}2$, etc.	$222 + \frac{1}{4}(220)$, etc.
36.	1.739	1.739	<1	653	$3\frac{5}{2}\frac{3}{2}$	$331 + \frac{1}{4}(0\bar{2}\bar{2})$
37.	1.703	1.703	1	661, 830	$33\frac{1}{2}$, etc.	$331 + \frac{1}{4}(00\bar{2})$, etc.
38.	1.693	1.692	<1	743, 750, 831	$\frac{7}{2}2\frac{3}{2}$, etc	$422 + \frac{1}{4}(\bar{2}0\bar{2})$, etc.
39.	1.682	1.680	<1	555, 751	$\frac{5}{2}\frac{5}{2}\frac{5}{2}$, etc.	$222 + \frac{1}{4}(222)$, etc.
40.	1.669	1.669	2	662	331	331
41.	1.617	1.617	3	663, 744, 900	$33\frac{3}{2}$, etc.	$331 + \frac{1}{4}(002)$, etc.
42.	1.543	1.543	7	850, 762, 843, 922	$4\frac{5}{2}0$, etc.	$420 + \frac{1}{4}(020)$, etc.
43.	1.486	1.485	14	844	422	422
44.	1.421	1.420	—	854, 1021	$4\frac{5}{2}2$, etc.	$422 + \frac{1}{4}(020)$, etc.
45.	1.400	1.400	—	666, 1022	333, etc.	333, etc.
46.	1.369	1.369	—	944, 870, 1032	$\frac{9}{2}22$, etc.	$422 + \frac{1}{4}(200)$, etc.

The XRD satellite data for the primitive cubic phase at $x = 0.55$ are dominated by $\frac{1}{4}\{220\}^*$- and $\frac{1}{4}\{002\}^*$-type modulation waves (see Table 6 and Fig. 4), with some relatively weaker $\mathbf{G} \pm \frac{1}{4}\{222\}^*$-type and $\mathbf{G} \pm \frac{1}{4}\{024\}^*$-type (labeled D) reflections. The primitive orthorhombic phase occurring at $x = 0.75$ and 0.85 gives the most complex pattern of satellite reflections with all the previously mentioned satellite types being observed and none of them dominant in relative intensity.

It is interesting to compare the satellite XRD data for low carnegieite ($x = 1.0$) with the orthorhombic phase

TABLE 7
XRD Data for $x = 0.85$ in the System $Na_{2-x}Al_{2-x}Si_xO_4$, $0 \le x \le 1$). Orthorhombic, $Pc2_1b$, $a = \sqrt{2}a_p = 10.308(1)$, $b = 2b_p = 14.226(7)$, $c = \sqrt{2}c_p = 10.214(2)$ Å

No.	d_{obs} Å	d_{calc} Å	I/I_0	hkl	hkl_p	$\mathbf{G} + \mathbf{q}$
1.	7.24	7.26	2	101	001	$000 + \frac{1}{2}(002)$
2.	6.47	6.46	5	111	$0\frac{1}{2}1$	$000 + \frac{1}{4}(024)$
3.	5.86	5.85	5	120	$\frac{1}{2}1\frac{1}{2}$	$111 - \frac{1}{4}(202)$
4.	5.08	5.08	2	121	011	$111 - \frac{1}{2}(200)$
5.	4.58	4.58	3	102	$-\frac{1}{2}0\frac{3}{2}$	$002 + \frac{1}{4}(\bar{2}0\bar{2})$
6.	4.17	4.17	100	220	111	111
7.	4.15	4.15	100	022	$\bar{1}11$	$\bar{1}11$
8.	3.97	3.97	2	131	$0\frac{3}{2}1$	$020 + \frac{1}{4}(0\bar{2}4)$
9.	3.85	3.85	5	122	$-\frac{1}{2}1\frac{3}{2}$	$\bar{1}11 + \frac{1}{4}(202)$
10.	3.47	3.47	4	032	$\bar{1}\frac{3}{2}1$	$\bar{1}11 + \frac{1}{4}(020)$
11.	3.36	3.36	3	140	$\frac{1}{2}2\frac{1}{2}$	$020 + \frac{1}{4}(202)$
12.	3.30	3.30	5	231	$\frac{1}{2}\frac{3}{2}\frac{3}{2}$	$111 + \frac{1}{4}(\bar{2}22)$
13.	2.88	2.88	4	232	$0\frac{3}{2}2$	$022 + \frac{1}{4}(0\bar{2}0)$
14.	2.85	2.85	1	302	$\frac{1}{2}0\frac{5}{2}$	$022 + \frac{1}{4}(202)$
15.	2.81	2.81	7	241	$\frac{1}{2}2\frac{3}{2}$	$022 + \frac{1}{4}(20\bar{2})$
16.	2.64	2.64	2	223	$-\frac{1}{2}1\frac{5}{2}$	$\bar{1}13 + \frac{1}{4}(20\bar{2})$
17.	2.58	2.58	25	400	202	202
18.	2.55	2.55	23	004	$\bar{2}02$	$\bar{2}02$
19.	2.54	2.54	35	242	022	022
20.	2.486	2.486	2	052	$\bar{1}\frac{5}{2}1$	$\bar{1}31 + \frac{1}{4}(0\bar{2}0)$
21.	2.443	2.443	15	332	$\frac{1}{2}\frac{3}{2}\frac{5}{2}$	$113 + \frac{1}{4}(\bar{2}2\bar{2})$
22.	2.419	2.419	7	303	003	$002 + \frac{1}{2}(002)$
23.	2.347	2.341, 2.358	<1	124, 421	$-\frac{3}{2}1\frac{5}{2}$, $\frac{3}{2}1\frac{5}{2}$	$\bar{1}13 + \frac{1}{4}(\bar{2}0\bar{2})$, $113 + \frac{1}{4}(20\bar{2})$
24.	2.238	2.239	3	252	$0\frac{5}{2}2$	$022 + \frac{1}{4}(020)$
25.	2.107	2.108	2	261	$\frac{1}{2}3\frac{3}{2}$	$131 + \frac{1}{4}(\bar{2}02)$
26.	2.089	2.087	3	440	222	222
27.	2.074	2.074	3	044	$\bar{2}22$	$\bar{2}22$
28.	2.034	2.034	2	413	$\frac{1}{2}1\frac{7}{2}$	$113 + \frac{1}{4}(\bar{2}\bar{2}2)$
29.	2.010	2.010	2	253	$-\frac{1}{2}\frac{5}{2}\frac{5}{2}$	$\bar{1}33 + \frac{1}{4}(2\bar{2}\bar{2})$
30.	1.894	1.895	2	512	$\frac{3}{2}1\frac{7}{2}$	$113 + \frac{1}{4}(2\bar{2}2)$
31.	1.879	1.878, 1.881	1	451, 334	$\frac{3}{2}\frac{5}{2}\frac{5}{2}$, $-\frac{1}{2}\frac{3}{2}\frac{7}{2}$	$133 + \frac{1}{4}(2\bar{2}\bar{2})$, $\bar{1}13 + \frac{1}{4}(222)$
32.	1.859	1.859	1	531	$2\frac{3}{2}3$	$222 + \frac{1}{4}(0\bar{2}\bar{4})$
33.	1.846	1.846	1	135	$\bar{2}\frac{3}{2}3$	$\bar{2}22 + \frac{1}{4}(0\bar{2}\bar{4})$
34.	1.821	1.820	2	263	$-\frac{1}{2}3\frac{5}{2}$	$\bar{1}33 + \frac{1}{4}(20\bar{2})$
35.	1.814	1.814	2	404	004	004
36.	1.782	1.783	3	254	$\bar{1}\frac{5}{2}3$	$\bar{1}33 + \frac{1}{4}(0\bar{2}0)$
37.	1.779	1.778	5	080	040	040
38.	1.758	1.758	1	424	014	$024 + \frac{1}{2}(0\bar{2}0)$
39.	1.744	1.745	1	460	232	$242 + \frac{1}{2}(0\bar{2}0)$
40.	1.718	1.718	<1	600	303	$313 + \frac{1}{2}(0\bar{2}0)$
41.	1.670	1.670	3	620	313	313
42.	1.655	1.655	1	372	$\frac{1}{2}\frac{7}{2}\frac{5}{2}$	$133 + \frac{1}{4}(\bar{2}2\bar{2})$
43.	1.594	1.594	2	514	$\frac{1}{2}1\frac{9}{2}$	$115 + \frac{1}{4}(\bar{2}\bar{2}2)$
44.	1.577	1.577	2	471	$\frac{3}{2}\frac{7}{2}\frac{5}{2}$	$133 + \frac{1}{4}(22\bar{2})$
45.	1.529	1.529	3	454	$0\frac{5}{2}4$	$024 + \frac{1}{4}(020)$
46.	1.481	1.481	7	642	224	224
47.	1.472	1.472	8	246	$\bar{2}24$	$\bar{2}24$
48.	1.464	1.464	8	480	242	242
49.	1.459	1.459	—	633	$\frac{3}{2}\frac{3}{2}\frac{9}{2}$	$155 + \frac{1}{4}(22\bar{2})$
50.	1.407	1.407	—	482	143	$153 + \frac{1}{2}(0\bar{2}0)$
51.	1.393	1.393	—	426	$\bar{1}15$	$\bar{1}15$
52.	1.382	1.382	—	137	$-3\frac{3}{2}4$	$\bar{4}24 + \frac{1}{4}(4\bar{2}0)$
53.	1.371	1.371	—	2 10 0	151	151
54.	1.270	1.270	—	714	$\frac{3}{2}1\frac{11}{2}$	$115 + \frac{1}{4}(2\bar{2}2)$

TABLE 8
Unit Cell Dimensions

Composition (x)	Symmetry	a (Å)	b (Å)	c (Å)
0.0 (β—Ref. (2))	$Pna2_1$	5.3871(2)	7.0320(2)	5.2180(2)
0.0 (γ—Ref. (3))	$P4_12_12$	5.325	5.325	7.058
0.05	$P4_12_12$	5.2997(6)	5.2997(6)	7.0758(9)
0.15	$Pbca$	10.425(2)	14.282(3)	5.2127(9)
0.25	$Pbca$	10.416(3)	14.250(3)	5.2038(9)
0.35	$P4_12_12$	10.3872(7)	10.3872(7)	7.1589(8)
0.45[a]	$Pbca$	10.385(1)	14.198(3)	5.1925(6)
0.45[a] (1 line)	$P2_13$	14.547(–)	14.547(–)	14.547(–)
0.50[a] (7 lines)	$Pbca$	10.385(2)	14.193(5)	5.193(1)
0.50[a]	$P2_13$	14.557(2)	14.557(2)	14.557(2)
0.55	$P2_13$	14.553(1)	14.553(1)	14.553(1)
0.65[a]	$P2_13$	14.531(1)	14.531(1)	14.531(1)
0.65[a]	$Pc2_1b$	10.320(2)	14.254(5)	10.258(4)
0.75	$Pc2_1b$	10.320(2)	14.241(3)	10.232(3)
0.85	$Pc2_1b$	10.308(1)	14.226(7)	10.214(2)
1.0 (low—Ref. (14))	$Pb2_1a$	10.261(1)	14.030(2)	5.1566(6)
1.0 (high—Ref. (11))	$P2_13/F\bar{4}3m$	7.37(2)	7.37(2)	7.37(2)

[a] Overall composition from specimen within a two-phase region.

occurring at $x = 0.25$ and 0.45. The profiles appear *almost* identical in terms of peak position and relative intensity except for the presence of reflections labeled F in Fig. 4, corresponding to $\mathbf{q} = \mathbf{0}$ modulation waves. As will be discussed later, these reflections result from the lowering of symmetry relative to the orthorhombic phase at $x = 0.25$ and 0.45 which is associated with Si:Al ordering (14).

Finally, one further observation that can be made from inspection of Fig. 3 is the relative intensities of low angle ($< 20°2\theta$) data for each phase. Compositional modulation, i.e., Si:Al and/or Na:vacancy ordering in the present case, will contribute to the intensity of satellite reflections most strongly at low angle, whereas displacive modulation, i.e., patterns of rotation of $\langle 110 \rangle$ tetrahedral strings, will contribute most strongly at higher angle. The qualitative difference between the XRD profiles at low angle shown in Fig. 4 suggest that the phases at $x = 0.35$, 0.55, and 0.85 are likely to have some degree of compositional modulation associated with modulation waves other than $\mathbf{q} = \mathbf{0}$. Note that the Si:Al and Na:vacancy ordering in low-carnegieite ($x = 1.0$) is associated with a $\mathbf{q} = \mathbf{0}$ modulation wave and, therefore, only shows up in higher angle parent F-centered lattice reflections, labeled F in Fig. 4.

Electron Diffraction Data and Space Group Determination

As with previous electron diffraction studies of stuffed cristobalite structures (15, 19), specimens were highly susceptible to electron beam damage. This beam damage increased with decreasing silica content such that no useful

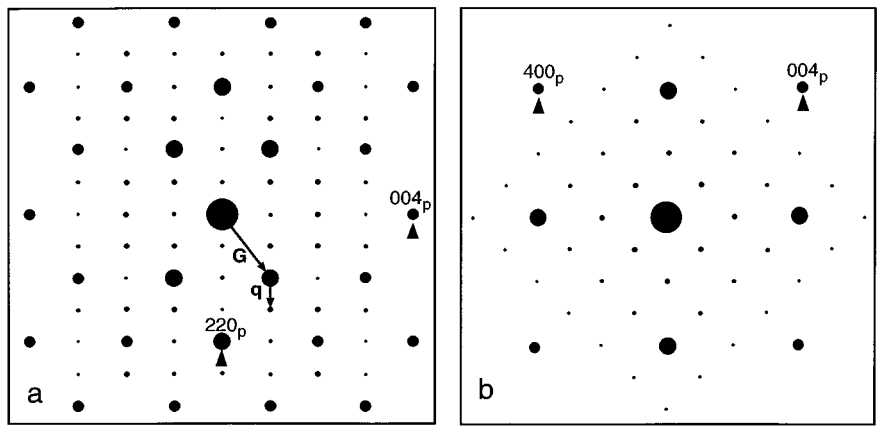

FIG. 5. Schematic representation of selected area electron diffraction patterns (SAEDPs) of the $x = 0.35$ specimen along the (a) [010] and (b) [$\bar{1}$10] zone axes for comparison with the observed SAEDPs in Figs. 6a and b. Satellite reflections (smaller filled circles) can be indexed as $\mathbf{G}_p \pm \mathbf{q}$, where $\mathbf{G}_p$ is an allowed $Fd\bar{3}m$ β-cristobalite-type parent structure reflection (larger filled circles) and $\mathbf{q}$ is a modulation wave-vector, e.g., $\mathbf{G}_p = 222$ and $\mathbf{q} = \frac{1}{4}(220)$ as shown in (a).

patterns were obtainable at $x = 0.05$. Consequently, it was not always possible to obtain selected area electron diffraction patterns (SAEDPs) along every major zone axis. Furthermore, twinning occurred quite commonly making it difficult to be sure that individual diffraction patterns were from single crystal regions. Given the underlying $Fd\bar{3}m$ β-cristobalite-type parent structure, this was only to be expected.

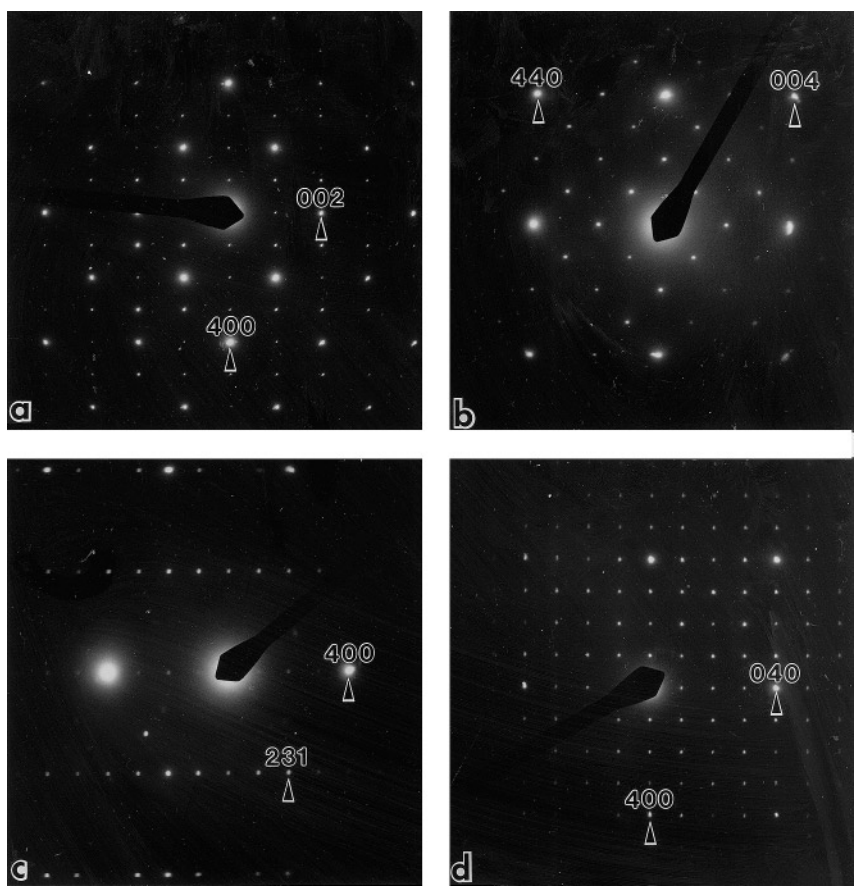

FIG. 6. Selected area electron diffraction patterns (SAEDPs) of the $x = 0.35$ specimen along the (a) [010], (b) [$\bar{1}$10], (c) [0$\bar{1}$3], and (d) [001] zone axes.

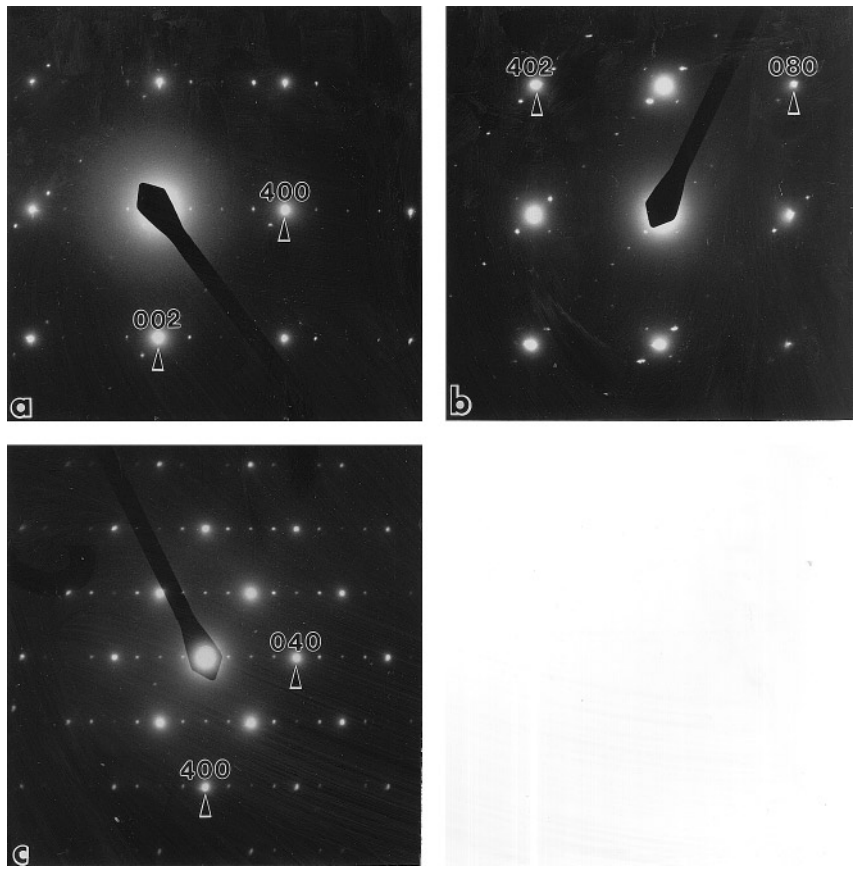

FIG. 7. Selected area electron diffraction patterns (SAEDPs) of the $x = 0.45$ specimen along the (a) [010], (b) [$\bar{1}$02], and (c) [001] zone axes.

Relevant SAEDPs are presented for $x = 0.35$ in Fig. 6, $x = 0.45$ in Fig. 7 (the $x = 0.25$ SAEDP's are identical), $x = 0.55$ in Fig. 8, and $x = 0.85$ in Fig. 9. The strong parent reflections labeled in each of these figures correspond to Bravais lattice allowed reflections of the underlying $Fd\bar{3}m$ β-cristobalite, or C9, type parent structure. In each case the unit cells as determined by powder XRD were confirmed, as was the primitive nature of the resultant Bravais lattice. In the following exposition the unit cells of the new phases can be visually related to the underlying $Fd\bar{3}m$ β-cristobalite-type parent structure by reference to the $[010]_p$ projection shown in Fig. 2.

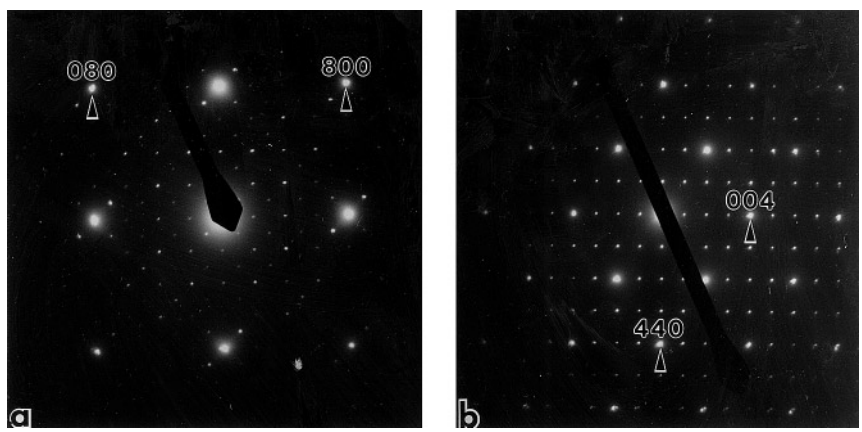

FIG. 8. Selected area electron diffraction patterns (SAEDPs) of the $x = 0.55$ specimen along the (a) [001] and (b) [$\bar{1}$10] zone axes.

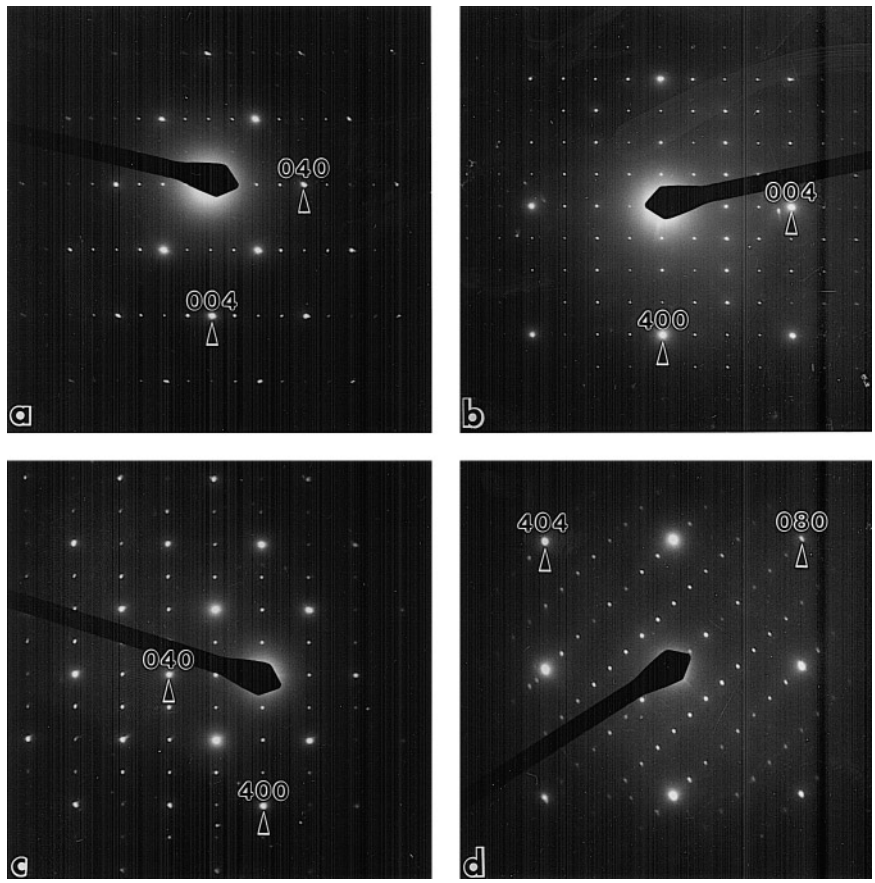

FIG. 9. Selected area electron diffraction patterns (SAEDPs) of the $x = 0.85$ specimen along the (a) [100], (b) [010], (c) [001], and (d) [$\bar{1}$01] zone axes.

Figure 6 shows (a) [010], (b) [$\bar{1}$10], (c) [0$\bar{1}$3], and (d) [001] SAEDP's characteristic of the $x = 0.35$ tetragonal ($\mathbf{a} = \mathbf{a}_p - \mathbf{b}_p$, $\mathbf{b} = \mathbf{a}_p + \mathbf{b}_p$, $\mathbf{c} = \mathbf{c}_p$; $\mathbf{a}^* = \frac{1}{4}(2\mathbf{a}_p^* - 2\mathbf{b}_p^*)$, $\mathbf{b}^* = \frac{1}{4}(2\mathbf{a}_p^* + 2\mathbf{b}_p^*)$, $\mathbf{c}^* = \frac{1}{2}(2\mathbf{c}_p^*)$) phase. No characteristic extinction conditions due to resultant glide planes perpendicular to the zone axis orientation are observed down either (a) $\langle 100 \rangle$, (b) $\langle 110 \rangle$, or (d) [001] zone axis directions. (Note that the detection of extinction conditions caused by the presence of screw axes perpendicular to the zone axis orientations of Fig. 6 is difficult as a result of the existence of strong multiple scattering routes into potential screw axis forbidden reflections.) Thus, formally, there exist 20 possible tetragonal space groups compatible with these observed extinction conditions (20).

Given an underlying $Fd\bar{3}m$ C9-type parent structure, however, the resultant derivative structure must be a subgroup thereof. Hence, the resultant structure cannot contain either a 4-fold or a 4_2 screw axis along **c**, a mirror plane perpendicular to **c** or a mirror plane perpendicular to the resultant tertiary, or $\langle 110 \rangle$, axes (refer to Fig. 2). These constraints rule out 13 of the above 20 possible resultant tetragonal space groups. The 7 remaining possibilities are $P4_1$, $P4_3$, $P4_122$, $P4_322$, $P4_12_12$, $P4_32_12$, or $P\bar{4}m2$. The virtual absence of $\mathbf{G}_p \pm \frac{1}{4}(2\mathbf{a}_p^* - 2\mathbf{b}_p^*)$ satellite reflections along the $(2\bar{2}0)_p^*$ direction of reciprocal space in Fig. 6c (where multiple scattering routes into the kinematically forbidden $2h+1, 0, 0$ reflections are minimized relative to Figs. 6a or 6c in conjunction with their strong presence for $\mathbf{G}_p$ not along the $(2\bar{2}0)_p^*$ direction of reciprocal space strongly suggests the existence of a 2_1 screw axis along the resultant secondary **a** and **b** axes. Such an interpretation is also consistent with the XRD results given in Table 4 and leads to possible resultant space groups of either $P4_12_12$ (No. 92) or $P4_32_12$ (No. 96).

Figure 7 shows (a) [010], (b) [$\bar{1}$02], and (c) [001] zone axis SAEDP's characteristic of the $x = 0.45$ $KGaO_2$-related, orthorhombic ($\mathbf{a} = \mathbf{a}_p + \mathbf{c}_p$, $\mathbf{b} = 2\mathbf{b}_p$, $\mathbf{c} = \frac{1}{2}(-\mathbf{a}_p^* + \mathbf{c}_p)$; $\mathbf{a}^* = \frac{1}{4}(2\mathbf{a}_p^* + 2\mathbf{c}_p^*)$, $\mathbf{b}^* = \frac{1}{4}(2\mathbf{b}_p^*)$, $\mathbf{c}^* = \frac{1}{2}(-2\mathbf{a}_p^* + 2\mathbf{c}_p^*)$) phase. The condition $F(h0l) = 0$ unless l is even (Fig. 7a) requires a resultant c glide perpendicular to **b** while the condition $F(hk0) = 0$ unless h is even (Fig. 7c) requires the presence of an a glide perpendicular to **c**. The resultant space group is thus necessarily of the form P–ca. There are 5 compatible orthorhombic space groups—namely $P2_1ca$,

Pmca, *Pbca*, *Pcca* or *Pnca*. (Unfortunately a [100] zone axis SAEDP, which could easily have distinguished between these various possibilities, was not obtained.) The strong and unambiguous presence of the 021 reflection (see Table 5), corresponding to the parent $\bar{1}11$ reflection, rules out the latter 2 possibilities. The XRD lines at 3.49, 2.491, and 2.275 Å (Table 5) are indexed to 230, 250, and 430, even though they might have been indexed as 031, 051, and 032, respectively, due to the fact that $c = \frac{1}{2}a$ exactly; i.e., despite the symmetry being orthorhombic, the underlying substructure remains metrically tetragonal. Thus, on the basis of extinction conditions alone, 3 possible resultant space groups remain—namely $P2_1ca$, *Pmca*, or *Pbca*.

As mentioned above, the extreme similarity between the $x = 0.25$ and $x = 0.45$ XRD patterns and that of the end-member $x = 1.0$ low carnegieite phase (see Figs. 3 and 4) requires a close structural relationship between these phases. In the case of low carnegieite, Withers and Thompson (14) have shown that the coupled tetrahedral edge rotations which generate the structure of low carnegieite from its underlying C9 parent structure have *Pbca* space group symmetry, as for $KGaO_2$. The actual space group symmetry of low carnegieite is reduced from *Pbca* to $Pb2_1a$ as a result of additional Al : Si and Na : vacancy ordering (corresponding to a $\mathbf{q} = \mathbf{0}$ compositional modulation) and associated structural relaxation (corresponding to a $\mathbf{q} = \mathbf{0}$ displacive modulation). It is this $\mathbf{q} = \mathbf{0}$ modulation that gives rise to the presence of the satellite reflections labeled F in the $x = 1.0$ low carnegieite XRD pattern of Fig. 4. The absence of the equivalent reflections in the $x = 0.25$ and $x = 0.45$ patterns of Fig. 4 represents the only substantive difference in the respective traces and suggests that the corresponding $\mathbf{q} = \mathbf{0}$ compositional modulation does not occur for $x = 0.25$ and $x = 0.45$; i.e., the appropriate resultant space group symmetry should be *Pbca*.

Figure 8 shows (a) [001] and (b) [$\bar{1}$10] zone axis SAEDP's characteristic of the $x = 0.55$ cubic ($\mathbf{a} = 2\mathbf{a}_p$, $\mathbf{b} = 2\mathbf{b}_p$, $\mathbf{c} = 2\mathbf{c}_p$; $\mathbf{a}^* = \frac{1}{4}(2\mathbf{a}_p^*)$, $\mathbf{b}^* = \frac{1}{4}(2\mathbf{b}_p^*)$, $\mathbf{c}^* = \frac{1}{4}(2\mathbf{c}_p^*)$) phase. Despite the cell being metrically cubic, there is always the possibility that the actual symmetry is lower. There was, however, never any evidence for broken cubic symmetry in electron diffraction patterns. The absence of extinction conditions at (a) $\langle 001 \rangle$ and (b) $\langle 110 \rangle$ zone axis orientations limits the possible resultant cubic space groups to 9. As described above for the $x = 0.35$ phase, however, one can further constrain the possible resultant space groups by requiring that they must be subgroups of the underlying $Fd\bar{3}m$ C9-type parent structure. Given its resultant unit cell, the structure cannot contain either 4-fold, 4_1, 4_2 or 4_3 screw axes along the primary **a**, **b**, or **c** axis directions or mirror planes perpendicular to these primary axes (refer to Fig. 2). These constraints rule out 6 of the above 9 possible resultant cubic space groups. The 3 remaining possibilities are *P*23, $P2_13$, or $P\bar{4}3m$. The virtual absence of the 300 and 500 reflections in Fig. 7a suggests the presence of a 2_1 screw along the primary **a**, **b**, and **c** directions (stronger multiple scattering routes into the observed 100 and 700 reflections exist) and makes us lean toward $P2_13$ as the most probable resultant space group although either of the other 2 possibilities cannot be definitively ruled out.

Finally, Fig. 9 shows (a) [100], (b) [010], (c) [001], and (d) [$\bar{1}$01] SAEDP's characteristic of the $x = 0.85$ orthorhombic ($\mathbf{a} = \mathbf{a}_p + \mathbf{c}_p$, $\mathbf{b} = 2\mathbf{b}_p$, $\mathbf{c} = (-\mathbf{a}_p + \mathbf{c}_p)$; $\mathbf{a}^* = \frac{1}{4}(2\mathbf{a}_p^* + 2\mathbf{c}_p^*)$, $\mathbf{b}^* = \frac{1}{4}(2\mathbf{b}_p^*)$, $\mathbf{c}^* = \frac{1}{4}(-2\mathbf{a}_p^* + 2\mathbf{c}_p^*)$) phase. The observed extinction conditions $F(0kl) = 0$ unless l is even and $F(hk0) = 0$ unless k is even (see Figs. 8a and c) in conjunction with the absence of an observed condition at the [010] zone axis orientation requires the resultant space group symmetry to be either $Pc2_1b$ (No. 29) or *Pcmb* (No. 57). A mirror plane perpendicular to the resultant **b** axis, however, is not compatible with an underlying $Fd\bar{3}m$ C9-type parent structure (refer to Fig. 2). The resultant space group can therefore be unambiguously determined to be $Pc2_1b$ (No. 29).

Trends in Unit Cell Dimensions

As all the crystalline phases observed in the system ($Na_{2-x}Al_{2-x}Si_xO_4$, $0 \le x \le 1$) have a common parent structure it is possible to relate their unit cell dimensions by appropriate changes in setting and/or scaling.

Figure 10 presents the normalized unit cell dimensions as a function of composition with solid solutions indicated by lines and two-phase regions by shaded rectangles. What is immediately evident is the approximately linear change for all but the normalized b dimension, where there is a striking ($\sim$2.5%) discontinuity associated with the cubic $P2_13$ phase at $x \approx 0.5$–0.6, and a smaller ($\sim$0.7%) discontinuity for the tetragonal $P4_12_12$ phase at $x \approx 0.35$ when observed against the dimension of the orthorhombic *Pbca* phase on either side of it. These discontinuities are preserved in the plot of normalized unit cell volume vs composition shown in Fig. 11. The decrease in dimension with increasing x is consistent, at least qualitatively, with the progressive substitution of Al by Si in the tetrahedral framework sites.

The distortion of β-cristobalite-related structures from their underlying parent structure is characterized by coupled rotation of $\langle 110 \rangle$ strings of tetrahedra about the tetrahedral edge normal to the string. The associated collapse of the unit cell dimensions normal to the rotation axis depends on the magnitude of the rotation angle (refer to Ref. (19)). While the actual unit cell dimensions and symmetries of the phases vary significantly with composition, the approximate continuity of normalized dimensions across phase boundaries indicates that all these structures undergo a similar magnitude of collapse. In each case the angles of rotation must be $\sim 20^\circ$. Both the concerted rotation and the associated collapse in unit cell dimensions can be seen in

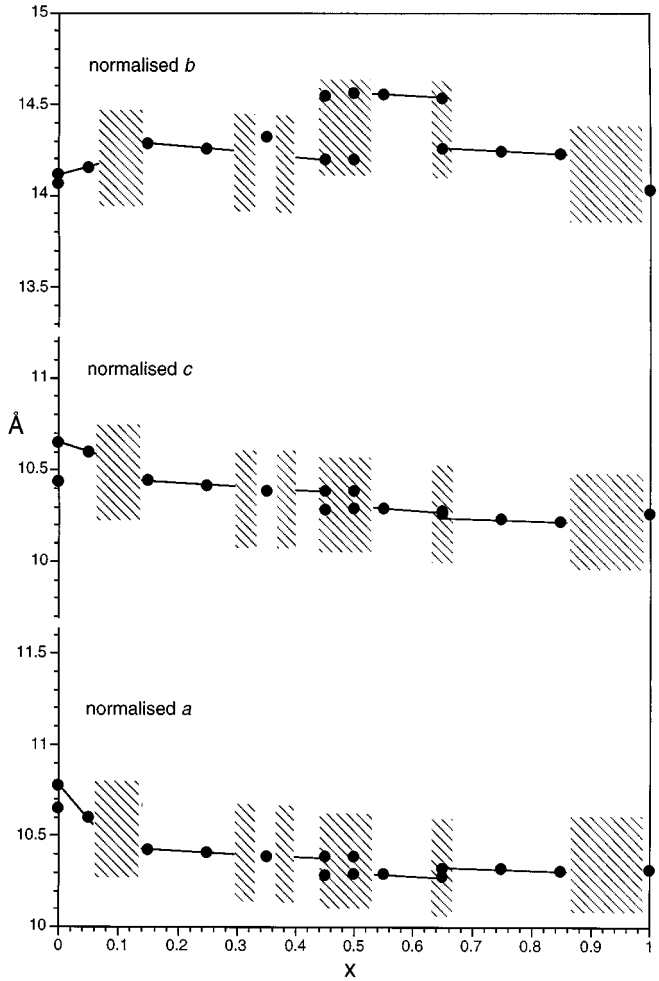

FIG. 10. Plot of the normalized refined unit cell dimensions for the system ($Na_{2-x}Al_{2-x}Si_xO_4$, $0 \le x \le 1$). The b and c axes for the tetragonal space groups have been interchanged and the dimensions scaled to allow comparison on the basis of a $\sqrt{2}a_p$, $\sqrt{2}b_p$, $2c_p$ unit cell. The shading indicates two-phase regions and the lines solid solutions. Errors in the data are significantly smaller than the filled circles representing the data points.

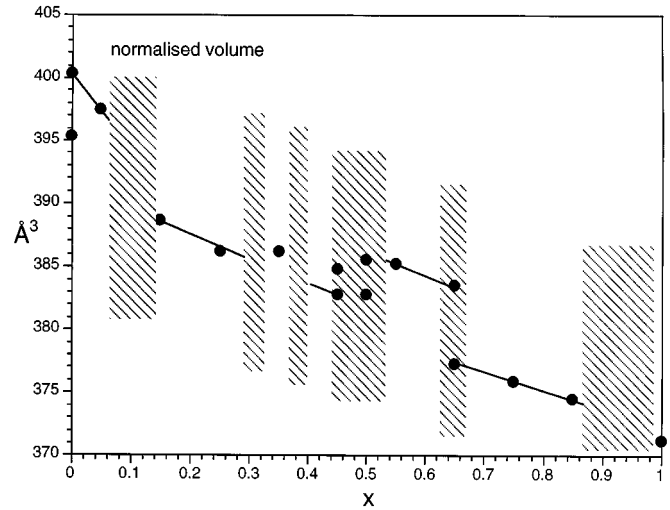

FIG. 11. Plot of the normalized refined unit cell volume for the system ($Na_{2-x}Al_{2-x}Si_xO_4$, $0 \le x \le 1$) (as described in the legend for Fig. 10).

Fig. 1 for the known end-member structures low-carnegieite (a) and β-$NaAlO_2$ (c) with respect to undistorted β-cristobalite (b). In Fig. 1 the relevant $\langle 110 \rangle$ strings of tetrahedra are delineated by dashed lines.

What is also noticeable in comparing Figs. 1a and 1c is that, while the angle of rotation is approximately the same, the pattern of rotation is different. So, while the structures of the five new phases reported in this study have yet to be solved and refined, their unit cell dimensions require that they must all have similar angles of rotation while their symmetries require the patterns of rotation to be different.

Proposed Composition Phase Relationships at 1300°C

The two main difficulties in determining a temperature vs composition equilibrium phase diagram for this pseudo-binary system were sluggish reaction kinetics at temperatures below $\sim$1300°C and significant sodium loss above $\sim$1300°C. Loss of sodium due to overheating of specimens was signaled by the emergence of the characteristic 11.3 and 5.65 Å diffraction lines of β-alumina in the XRD pattern (21), indicating deviation from the binary join. A specimen was judged at or close to equilibrium by sharpening of lines, lack of significant change with further heating, the ability to index all lines to one or two phases, and reproducibility of the experiment. Unfortunately, as we were limited to use of unsealed vessels for this study, we are effectively limited to presenting a composition-only phase diagram at $\sim$1300°C.

Figure 12 shows the phase relationships at 1300°C in the system ($Na_{2-x}Al_{2-x}Si_xO_4$, $0 \le x \le 1$) using the data obtained in the present study and from the literature for the end members. Comparison with the temperature vs composition diagram reported for the $NaFeO_2$–SiO_2 system for 0–20 mol% SiO_2 (5) shows several similarities. In this system the γ_{ss} phase is observed up to $\sim$5 mol% SiO_2, a γ'_{ss} phase is observed from $\sim$7.5 to $\sim$20 mol% SiO_2 (and to at least 25 mol% according to the text), with a $\gamma_{ss} + \gamma'_{ss}$ two-phase region in between. Comparison of unit cells, space groups and relative intensities indicate that our tetragonal phase observed at $x = 0.05$ is isostructural with the γ_{ss} phase, and therefore is also isostructural with α-cristobalite, and that our orthorhombic phase observed at $x = 0.25$ and 0.45 is isostructural with the γ'_{ss} phase, and therefore also with $KGaO_2$ and $Na_{1.74}Mg_{0.79}Al_{0.15}Si_{1.06}O_4$ (19).

The tetragonal phase at $x \approx 0.35$, the cubic phase at $x \approx 0.5$–0.6 and the orthorhombic phase at $x \approx 0.7$–0.9 are all apparently without precedent in analogous systems. The region between $x \approx 0.9$ and $x = 1.0$ can only be inferred as

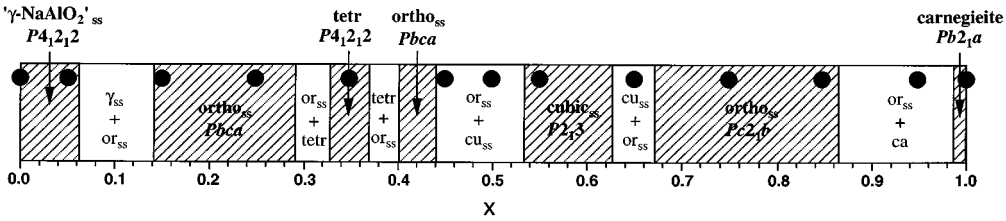

FIG. 12. Proposed composition phase diagram at 1300°C for the system ($Na_{2-x}Al_{2-x}Si_xO_4$, $0 \leq x \leq 1$). The filled circles show the compositions studied.

equilibrium was never obtained at compositions $x = 0.95$ and 1.0 using the present synthesis methods.

CONCLUSIONS

The phase diagram proposed by Schairer and Bowen (1) implied a continuous solid solution extending between the end members sodium aluminate and carnegieite, both of which have β-cristobalite-related structures. The five new phases at intermediate compositions reported in this study also have β-cristobalite-related structures, so in one sense Schairer and Bowen were right. The rich detail of the system ($Na_{2-x}Al_{2-x}Si_xO_4$, $0 \leq x \leq 1$) which they missed has only been accessible by combining careful synthesis with thorough characterization using XRD and electron diffraction. In particular, our previous studies of low-carnegieite (14, 15) and β-cristobalite-related sodium magnesiosilicates (19) and the earlier work of Grey and Li on the $NaFeO_2$–SiO_2 system (5) sensitized us to the subtle differences which distinguish the various phases in the present system.

The difficulty in achieving equilibrium in the system ($Na_{2-x}Al_{2-x}Si_xO_4$, $0 \leq x \leq 1$) due to sluggish kinetics cannot be overemphasized. For this reason we concede that our proposed composition phase diagram is incomplete, particularly toward the carnegieite composition. Furthermore, it only describes the phase relationships of specimens quenched to room temperature from 1300°C. It is quite possible that reversible nonreconstructive phase transitions occur for the intermediate phases in the same way that they occur for the end members, i.e., γ- $\rightarrow$ β-$NaAlO_2$, high- $\rightarrow$ low-carnegieite, and that we have only observed the low-temperature structures.

Nevertheless, this study has added at least three new structure types to the growing list of β-cristobalite-related phases. Work is now in progress to solve and refine the structures of all five new phases from the XRD data using the Rietveld method and starting models derived from a modulation wave approach to the description of these phases.

REFERENCES

1. J. F. Schairer and N. L. Bowen, *Am. J. Sci.* **254**, 129 (1956).
2. J. A. Kaduk and S. Pei, *J. Solid State Chem.* **115,** 126 (1995).
3. J. Théry and D. Briancon, *Rev. Hautes Temp. Refract.* **1**, 221 (1964).
4. R. C. De Vries and W. L. Roth, *J. Am. Ceram. Soc.* **52**, 364 (1969).
5. I. E. Grey and C. Li, *J. Solid State Chem.* **69,** 116 (1987).
6. A. F. Reid and A. E. Ringwood, *Inorg. Chem.* **7**, 443 (1968).
7. J. Théry, A.-M. Lejus, D. Briancon, and R. Collongues, *Bull. Soc. Chim Fr.* 973 (1961).
8. A. J. Leadbetter, T. W. Smith, and A. F. Wright, *Nature* (*London*) **244,** 125 (1973).
9. P. P. Ewald and C. Hermann (Eds.), "Strukturbericht," Vol. I, pp. 169–171 (1913–1928).
10. W. Wong-Ng, H. F. McMurdie, B. Paretzkin, M. A. Kuchinski, and A.L. Dragoo, *Powder Diffr.* **3**, 246 (1988).
11. T. F. W. Barth and E. Posnjak, *Z. Kristallogr.* **81,** 135 (1932).
12. C. Hermann, O. Lohrmann, and H. Philipp (Eds.), "Strukturbericht", Vol. II, pp. 158–159 (1928–1932).
13. R. Klingenberg and J. Felsche, *J. Appl. Crystallogr.* **14**, 66 (1981).
14. R. L. Withers and J. G. Thompson, *Acta Crystallogr. Sect. B* **49,** 614 (1993).
15. J. G. Thompson, R. L. Withers, A. K. Whittaker, R. M. Traill, and J. D. Fitz Gerald, *J. Solid State Chem.* **104,** 59 (1993).
16. M. J. Buerger, *Am. Mineral.* **39**, 600 (1954).
17. I. E. Grey, B. F. Hoskins, and I. C. Madsen, *J. Solid State Chem.* **85,** 202 (1990).
18. J. Grins and D. Louër, *J. Solid State Chem.* **87,** 114 (1990).
19. R. L.Withers, C. J. Lobo, J. G. Thompson, S. Schmid, and R. Stranger, *Acta Crystallogr. Sect. B* **53,** 203–220 (1997).
20. T. Hahn (Ed.), "International Tables for Crystallography, Vol. A, Space Group Symmetry." Riedel, Dordrecht, 1983.
21. G. Yamaguchi and K. Suzuki, *Bull. Chem. Soc. Jpn.* **41**, 93 (1968).